

¹ A deep learning-based dual latent space method for the
² estimation of physical flow properties from fiber optic
³ measurements

⁴ Misael M. Morales^{1*}, Kostyantyn Kravchenko², Andrea Rosales², Alberto Mendoza², Michael
⁵ Pyrcz^{1,3}, and Carlos Torres-Verdín^{1,3}

⁶ 1. Hildebrand Department of Petroleum and Geosystems Engineering, The University of Texas at Austin

⁷ 2. Lytt Limited

⁸ 3. Jackson School of Geosciences, The University of Texas at Austin

⁹ *Corresponding author; email: misaelmorales@utexas.edu

¹⁰ **Abstract**

¹¹ Distributed fiber optic sensing (DFOS) technologies have emerged as cost-effective high-resolution monitoring
¹² alternatives over conventional geophysical techniques. However, due to the large volume and noisy nature
¹³ of the measurements, significant processing is required and expert, fit-for-purpose tools must be designed to
¹⁴ interpret and utilize DFOS measurements. Deep learning techniques provide the flexibility and efficiency to
¹⁵ process and utilize DFOS measurements to estimate subsurface energy resource properties. We propose a
¹⁶ deep learning-based dual latent space method to process distributed acoustic sensing (DAS) and distributed
¹⁷ temperature sensing (DTS) measurements and estimate the injection point location and relative multiphase
¹⁸ flow rates along a flow-loop equipped with a DFOS unit. The dual latent space method is composed of
¹⁹ two identical convolutional U-Net AutoEncoders to compress and reconstruct the DAS and DTS data,
²⁰ respectively. The AutoEncoders are capable of determining an optimal latent representation of the DAS
²¹ and DTS measurements, which are then combined and used to estimate the physical flow properties along
²² six different experimental trials. The predictions are obtained within 7 milliseconds and with over 99.98%
²³ similarity and less than 3.68×10^{-9} relative error. The method is also shown to be robust to noise, and can
²⁴ be applied to different multiphase scenarios with a single pre-training procedure. The proposed method is
²⁵ therefore capable of fast and accurate estimation of physical flow properties, and can be used for real-time
²⁶ monitoring in different subsurface energy resource applications.

²⁷ **Keywords:** Distributed fiber optic sensing, Flow properties estimation, Convolutional neural network,
²⁸ Latent space modeling.

29 1 Introduction

30 Distributed fiber optic sensing (DFOS) technology offers high-resolution measurements in harsh environments
31 where conventional electric sensors fail or are insufficient to provide detailed characterization of the
32 environment [1, 2]. DFOS units operate by laser pulses along a fiber that interacts with imperfections in
33 the glass and are back-scattered to the source and recorded by an interrogator [3]. DFOS units serve as a
34 possible solution for reliable, cost-effective, and detailed monitoring of complex flow systems [4, 5]. However,
35 though promising, this technique requires technological advances in processing and integration for useful
36 interpretation, monitoring, and prediction in subsurface energy systems.

37 Over the last decade, DFOS systems have gained attention and popularity in the energy resource industry
38 [6–9]. DFOS systems have also become increasingly available, reliable, and economical, resulting in their
39 broader adoption for a wide range of subsurface applications. The two main measurements in subsurface
40 energy resource applications are distributed acoustic sensing (DAS) and distributed temperature sensing
41 (DTS). DAS consists of continuous measurements of axial strain rate along the fiber using Rayleigh scattering
42 interferometry. On the other hand, DTS consists of continuous measurements of the temperature profile along
43 the length of the fiber using the Raman effect. Moreover, DAS and DTS measurements can be realized over
44 large distances by analyzing back-scattered signal frequency, intensity, and phase [10]. However, such high-
45 density spatiotemporal measurements can amount to several Terabytes of data, making them challenging to
46 process and analyze using standard techniques.

47 Machine learning (ML) techniques have emerged as candidate solutions to rapidly and efficiently process
48 and analyze DFOS measurements [11? , 12]. Due to the recent increase in computing power and storage
49 capacity available, ML techniques provide a significant advantage for understanding DFOS measurements.
50 More specifically, deep learning (DL) techniques based on neural network models have proven capable and
51 flexible to process DFOS measurements efficiently and provide accurate predictions of subsurface properties
52 [13, 14]. On the other hand, latent space modeling techniques have proven useful to extract salient information
53 from large datasets, providing a reduced-dimensionality representation of the features and accelerating
54 the processing workflow [15, 16].

55 Several attempts have been made in ML-based and DL-based techniques for DFOS processing and analysis
56 in the energy resources industry [17–19]. Bhattacharya et al. [20] were the first to compare different ML
57 techniques to predict hydrocarbon production from multiple data sources, including DFOS measurements.
58 They use DAS and DTS data to evaluate the well performance over time for a multi-stage stimulated gas
59 well in the Marcellus Shale. They show that different ML techniques are efficient and accurate in predicting
60 daily gas production compared to traditional highly-complex simulations, and that DFOS measurements

61 are sufficiently high in spatial and temporal resolution to provide accurate predictions of well performance.
62 However, their methodology focuses on incorporating pre-processed multi-source, multi-physics data to aid
63 a single prediction, rather than focusing on real-time processing of high-resolution DAS and DTS.

64 The application of DL-based techniques for subsurface monitoring and characterization using DFOS
65 measurements has also been widely explored [21, 22]. Sherman et al. [13] developed a physics-informed neural
66 network (PINN) to predict the physical properties of a hydraulic fracture from DAS measurements. Their
67 method consists of a three-part neural network: (1) a convolutional neural network (CNN) to parameterize
68 the DAS measurements, (2) an artificial neural network (ANN) to parameterize geometric factors such as x
69 and y locations, and (3) a second ANN to merge the two previous parameterizations and predict the hydraulic
70 fracture physical properties such as height and length. It is important to note that they pre-process the DAS
71 measurements and rescale and resample them into conformable units for the DL model. Moreover, their work
72 does not incorporate a spatial component for dynamic monitoring. Huot et al. [23] developed a DL-based
73 method for detection and characterization of microseismic events from DAS measurements. Their model
74 consists of a convolutional neural network to process DAS measurements and reconstruct the corresponding
75 microseismic response. They show that DAS measurements can be used as a replacement to expensive and
76 complex seismic surveys to provide high-resolution subsurface monitoring.

77 We propose a deep learning-based dual latent space model to estimate the physical flow properties of a
78 subsurface energy resource system from DFOS measurements. The dual latent space model is based on two
79 mirrored convolutional U-net AutoEncoders to compress and reconstruct the DAS and DTS measurements,
80 and a latent regression function to estimate the injection point location and relative multiphase flow rates at
81 each injection point. The method is tested using DFOS measurements from a flow-loop experiment consisting
82 of different trials with multiphase flow of oil, gas, water, and sand. Furthermore, we compare the efficiency
83 and accuracy of the method using the dual latent space model as opposed to a single latent space model,
84 and quantify the uncertainty in the estimation based on different levels of noise in the DFOS measurements.

85 Section 2 describes the design of the flow-loop experiments, data processing, and the architecture of
86 the dual latent space model. Section 3 shows the results for 6 different trials, as well as a comparison
87 against a single latent space model, and the uncertainty quantification for the flow parameter estimation.
88 Finally, Section 4 provides the conclusions, challenges, and future research opportunities for deep learning
89 applications in DFOS analysis.

90 **2 Methodology**

91 This section describes the design of the flow-loop experiments, the DFOS data processing, and the architec-
 92 ture of the dual latent space model.

93 **2.1 Flow-loop Experiment Design**

94 Given that supervised ML and DL models require labeled data for training, we rely on laboratory results from
 95 numerous flow-loop experiments. The flow-loop is designed with a specified distance between the injection
 96 points, and variable multiphase flow characteristics for background and injection points flow, namely the
 97 physical flow properties. A fiber optic cable is placed between the tubing and the casing to continuously
 98 record DAS and DTS measurements. Figure 1 shows a simplified diagram of the flow-loop design, adapted
 99 from [24].

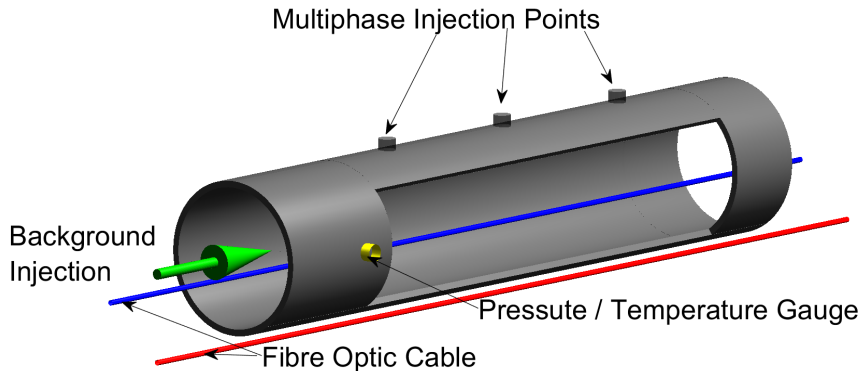


Figure 1: Schematic of multiphase flow-loop with DFOS unit for experimental data acquisition (for more experimental details see [25]).

100 The experiments are composed of 6 trials, where the background and injection point flow vary in terms
 101 of rate and phases. Table 1 summarize the 6 experimental trials. Similarly, Figure 2 shows a graphical
 102 representation of the multiphase flow rates for each trial, and their normalized values. Normalization is
 103 applied using *MinMax* scaling, such that:

$$\hat{x} = \frac{x - \min(x)}{\max(x) - \min(x)}, \quad (1)$$

104 where x represents the original data, and \hat{x} is the normalized data. The normalized data therefore lies in
 105 the range of $[0, 1]$. This is done to aid the deep learning nonlinear activation functions and backpropagation
 106 stability, and to obtain representative error metrics during the training process.

Table 1: Summary of multiphase flow rates for each of the 6 trials in the flow-loop experiments, expressed in the following units: oil (bpd), gas (cfd), water (bpd), sand (pptb).

	Trial 45				Trial 48			
	Oil	Gas	Water	Sand	Oil	Gas	Water	Sand
Background	1500	0	0	0	3000	0	0	0
Injection 1	250	8250	0	0	500	0	0	0
Injection 2	250	8250	0	0	150	0	1500	0
Injection 3	0	0	0	0	100	0	0	0
Injection 4	0	0	0	0	5000	0	0	0
	Trial 54				Trial 64			
	Oil	Gas	Water	Sand	Oil	Gas	Water	Sand
Background	1500	50000	0	0	3000	100000	0	0
Injection 1	250	8333.33	1000	0	250	8333.33	250	0
Injection 2	250	8333.33	0	0	250	8333.33	100	0
Injection 3	0	0	0	0	0	0	0	0
Injection 4	500	16666.66	1000	0	250	8333.33	250	0
	Trial 109				Trial 128			
	Oil	Gas	Water	Sand	Oil	Gas	Water	Sand
Background	6000	90000	0	0	3000	60000	0	0
Injection 1	500	7500	0	0	500	20000	0	0
Injection 2	500	7500	0	0	500	20000	0	0
Injection 3	0	0	0	0	0	0	0	0
Injection 4	0	0	500	10	500	20000	0	5

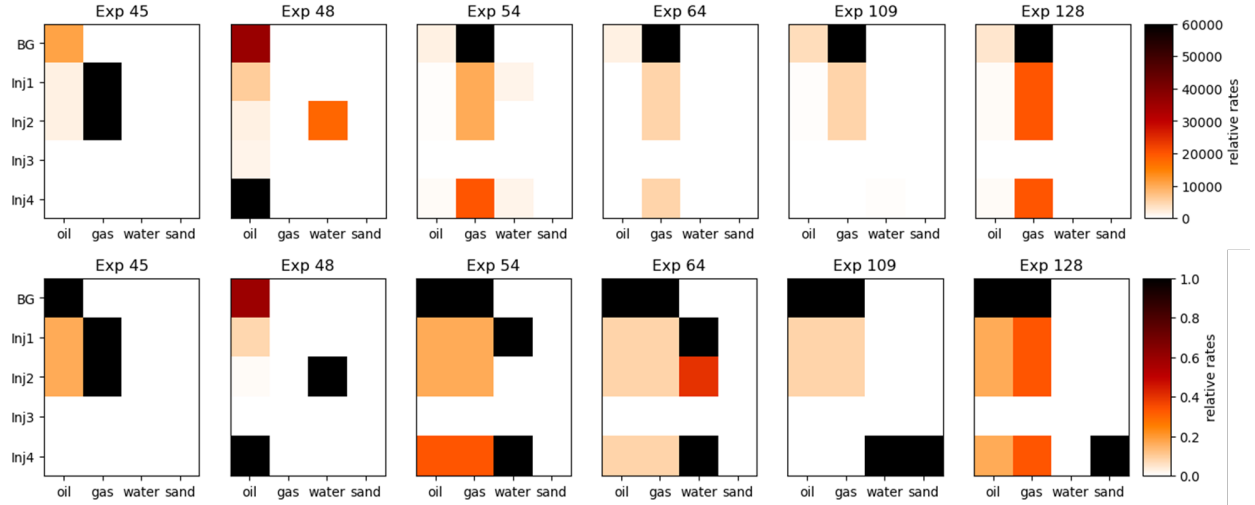


Figure 2: Visual representation of the multiphase flow rates for each of the 6 trials in the flow-loop experiments. The top row shows the multiphase flow rates in their original units, and the bottom row shows the normalized flow rates.

107 2.2 Data Processing

108 The DAS and DTS measurements for each experimental trial consists of approximately 100 Gb of data.
 109 Therefore, significant data processing is required to crop and rescale the DAS and DTS measurements into
 110 manageable sizes that retain all the significant information.

111 During the experiments, the fiber optic cable has a total length of 5,504 meters. This is to represent
 112 the approximate depth of a well and to account for signal loss and attenuation of the DFOS measurements
 113 across the depth interval of production. The majority of the fiber optic cable lies outside the flow-loop
 114 since the flow-loop has approximately under 200 meters in length. Thus, we crop the raw data to a 200
 115 meter window around the flow-loop. This significantly reduces the dimensionality of the data and allows
 116 for more manageable processing and inference. Furthermore, we match the injection point locations to their
 117 corresponding distance along the flow-loop to make a sparse representation of the injection point location
 118 and relative multiphase flow rate for each trial. Figure 3 shows the relative multiphase flow rates for each of
 119 the 6 trials within the significant window of the flow-loop.

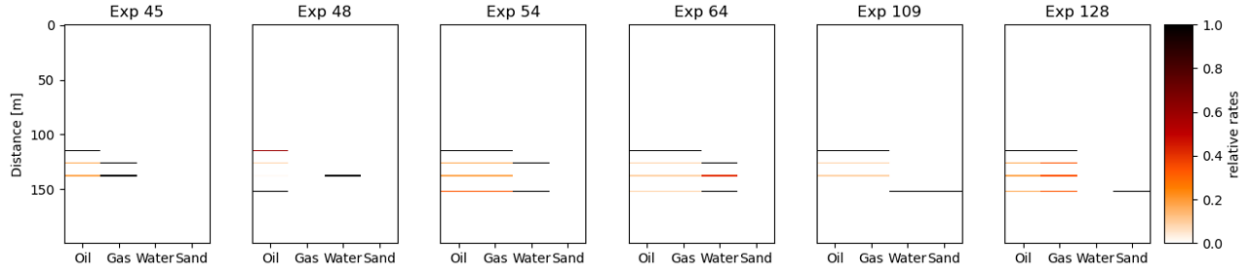


Figure 3: Relative multiphase flow rate and injection point location for each of the 6 trials in the experiment.

120 Each experimental trial is run for a slightly different time length, resulting in measurement data of differ-
 121 ent sizes. Moreover, the DAS and DTS interrogators record temporal measurements at different frequencies,
 122 also resulting in measurement data of different sizes. For example, Trial 1 has approximately 108,000
 123 DAS temporal measurements and 78 DTS temporal measurements, and Trial 6 approximately 126,000 DAS
 124 temporal measurements and 93 DTS temporal measurements. These invalidate the requirements for training
 125 deep learning models, where each sample must have the same dimensions as the others in terms of spatial and
 126 temporal coordinates. To tackle this, we apply a smart sampling strategy using Latin Hypercube Sampling
 127 (LHS) [26].

128 Let d_A represent the DAS data for a given experimental trial, and d_T represent the DTS data. The
 129 dimensions of d_A and d_T are given by (m_A, n_A) and (m_T, n_T) , respectively. Let m represent the spatial
 130 dimension, and n represent the temporal dimension. Recall that we crop the spatial dimension to a 200-
 131 meter window centered along the flow-loop. Thus, $m_A = m_T = 200$. To normalize the temporal coordinates,
 132 we resample the DAS measurements to the same frequency as the DTS measurements using LHS. This
 133 allows for representative sampling of the DAS signal at the same frequency as the DTS signal, without
 134 decimating or aliasing the DAS measurements. Now, for each trial in the experiment, $n_A = n_T = n$, where
 135 n can vary between experiments. Figure 4 shows the processed, resampled, and normalized DAS and DTS
 136 measurements for two sample trials in the experiment.

137 The resulting processed data is significantly reduced in magnitude compared to the raw DFOS measure-
 138 ments. In terms of dimensionality, DAS is compressed from approximately (5504, 100000) to approximately
 139 (200, 80), resulting in a 0.003% compression ratio (CR), calculated as:

$$CR = \frac{\text{reduced data dimensionality}}{\text{original data dimensionality}} \times 100\%. \quad (2)$$

140 Similarly, the processed data is significantly smaller in magnitude in terms of physical memory compared
 141 to the raw DFOS measurements. While the original DAS measurements occupy approximately 100 Gb of
 142 memory, the processed DAS data is only 1.56 Gb. The exact compression ratio and data magnitude reduction

143 depends on the initial dimensionality of the experimental trial, but in general a noteworthy compression is
 144 achieved for all trials.

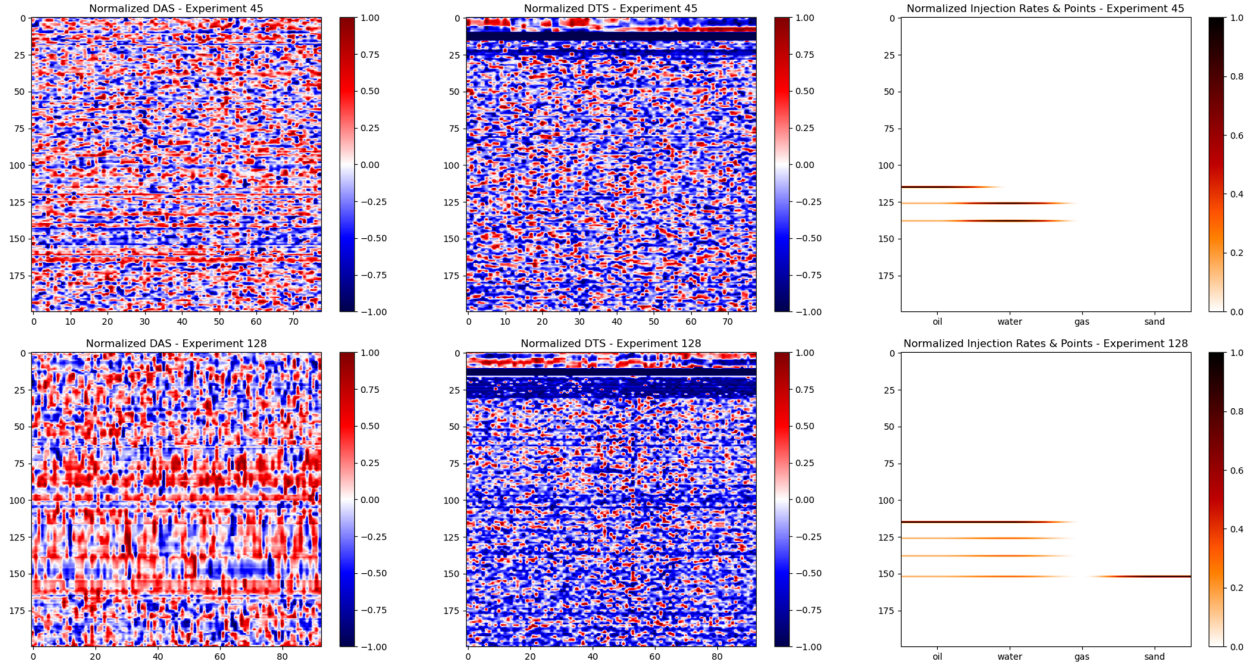


Figure 4: Visualization of the DAS (left), DTS (center) and physical flow properties (right) for two trials in the experiment. The top row shows Experiment 45, and the bottom row shows Experiment 128.

145 2.3 Model Architecture

146 AutoEncoders (AE) are a type of semi-supervised deep learning architecture that compress, or encode, the
 147 original data, X , into a latent representation z , and then use a mirror architecture of the encoder, called
 148 a decoder, to reconstruct the data into \hat{X} . Figure 5 shows a simple representation of an AE architecture.
 149 The goal is to minimize the differences between X and \hat{X} by optimizing the parameters within the Encoder
 150 (Enc) and Decoder (Dec) portions of the network. AEs can be expressed as follows:

$$\hat{X} = Dec(Enc(X)) = Dec(z) \quad (3)$$

151 such that $\min(\hat{e})$, where $\hat{e} = ||X - \hat{X}||$. A perfect AE will result in loss-less compression of the data X ,
 152 such that $\hat{X} \equiv X$. However, in practice, we will always obtain a lossy compression of X , such that $\hat{X} \approx X$.
 153 This is not necessarily bad, since the latent representation, z , might contain sufficient information about X
 154 to estimate or predict our quantity of interest (e.g., physical flow properties) when X is excessively large.

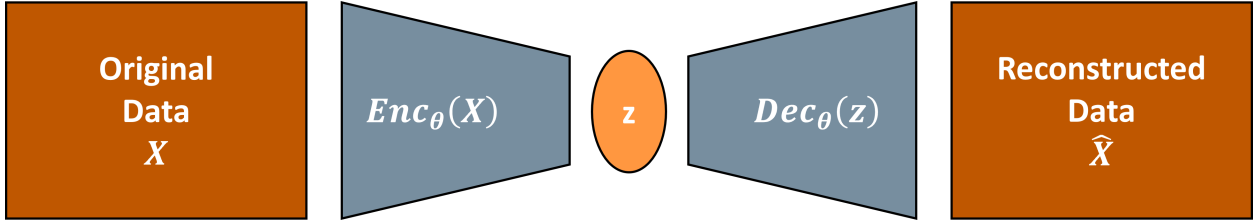


Figure 5: Simplified schematic of an AutoEncoder model. The original data, X , is encoded into a latent representation, z , and then decoded using a mirror image of the encoder to reconstruct the data, \hat{X} .

155 A convolutional U-Net AutoEncoder [27], is a specific AE architecture where the hidden layers consist of
 156 convolutions and residual concatenations at each hidden layer between the mirrored Encoder and Decoder
 157 portions. Figure 6 shows a simplified schematic of a convolutional U-Net AutoEncoder architecture.

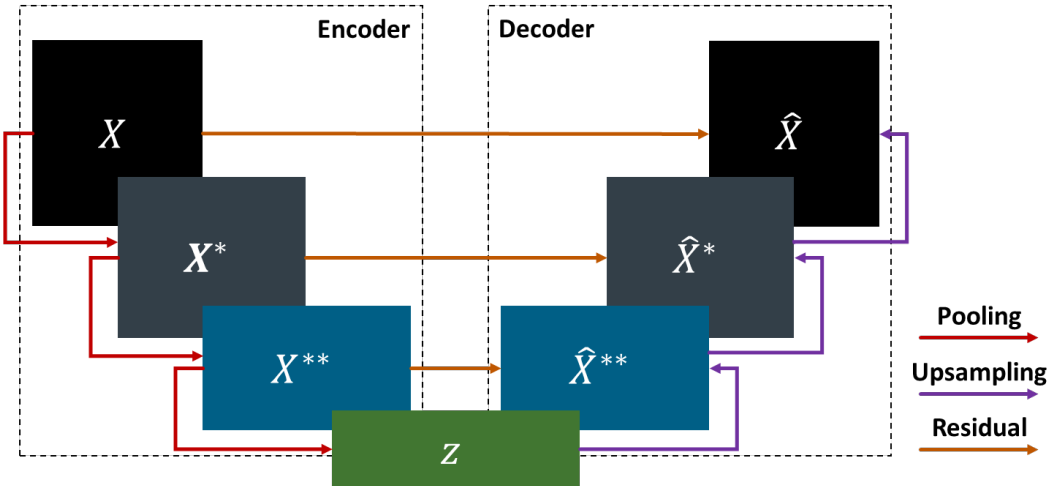


Figure 6: Schematic of a convolutional U-Net AutoEncoder architecture. The original data, X , is encoded into a latent representation, z , and a mirror Decoder reconstruct the original data into \hat{X} . Residual concatenations connect each mirrored hidden layer between the Encoder and Decoder portions of the network.

158 Each convolutional U-Net AutoEncoder is composed of four encoding layers and four mirroring decoding
 159 layers. In each encoding layer we perform two repeated padded convolutions and batch normalization, with
 160 a LeakyReLU activation function and a max pooling. The four encoding layers have filter sizes of 4, 16,
 161 32, and 64, respectively. On the other hand, each decoding layer is composed of a transposed convolution
 162 followed by a residual concatenation and two repeated padded convolutions and batch normalization with
 163 LeakyReLU activation. Mirroring the encoding layers, the four decoding layers have filter sizes of 64, 32, 16,
 164 and 4, respectively. Figure 7 shows the detailed schematic of each encoding and decoding layer.

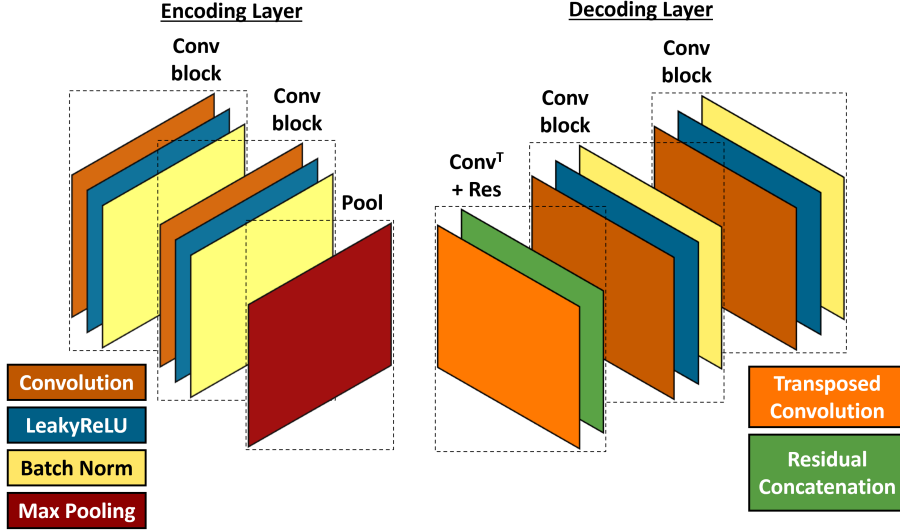


Figure 7: Detailed schematic of each encoding (left) and decoding (right) layer in the convolutional U-Net AutoEncoder architecture.

165 Our proposed dual latent space method merges two convolutional U-Net AutoEncoders into a single
 166 framework. The first AE compresses and reconstructs the DAS measurements, and the second AE compresses
 167 and reconstructs the DTS measurements. Both AEs are identical to each other, but trained separately to
 168 capture the distinct features that are intrinsic to each separate data source. We pre-train each AE to
 169 optimally compress and reconstruct the DAS and DTS measurements, respectively. This ensures that the
 170 latent representations obtained from each AE will optimally represent the DAS and DTS data, respectively.
 171 This procedure can be expressed as follows:

$$z_i = Enc_{\theta_i}(X_i), \quad (4)$$

$$\hat{X}_i = Dec_{\psi_i}(Enc_{\theta_i}(X_i)) = Dec_{\psi_i}(z_i), \quad (5)$$

172 where $i = \{DAS, DTS\}$, and θ_i and ψ_i are the Encoder and Decoder loss for the DAS and DTS AEs,
 173 respectively.

174 We extract only the Encoder portions of each AE and use the obtained latent representations, z_i , to
 175 construct a dual latent space, namely z^* , from the concatenation of the DAS and DTS latent spaces such
 176 that $z^* = [z_{DAS}, z_{DTS}]$. The physical flow properties, y , are then estimated using a latent regressor, f , such
 177 that $y = f(z^*)$. Figure 8 shows the architecture to estimate the physical flow properties from the dual latent
 178 space using the pre-trained DAS and DTS Encoders only. Figure 9 shows the complete architecture for our
 179 dual latent space method.

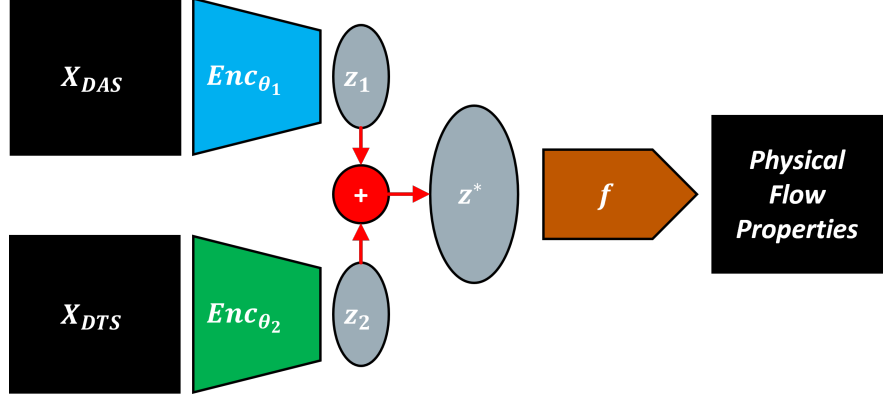


Figure 8: Schematic of the dual latent space method to estimate physical flow properties from DAS and DTS measurements. The pre-trained DAS (blue) and DTS (green) encoders are used to generate their corresponding latent spaces, which are combined into z^* and used to predict the physical flow properties, y , with a latent regressor, f .

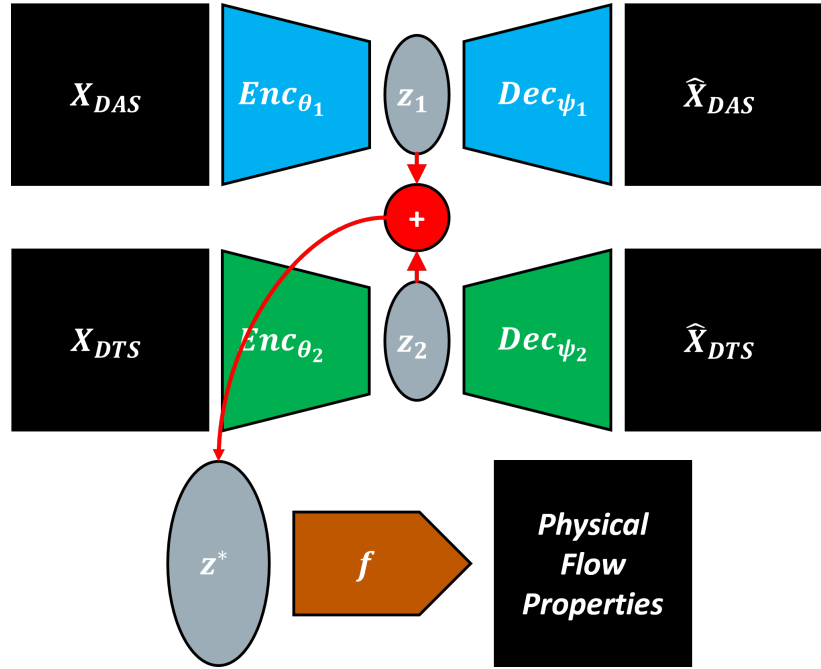


Figure 9: Schematic of the complete dual latent space model architecture. The DAS AE encodes X_{DAS} into z_1 and decodes to reconstruct \hat{X}_{DAS} (blue). The DTS AE encodes X_{DTS} into z_2 and decodes to reconstruct \hat{X}_{DTS} (green). The two latent spaces, z_1 and z_2 , are combined into a dual latent space, z^* , which is used to predict the physical flow properties, such that $y = f(z^*)$.

181 3 Results

182 This section describes the training performance and prediction accuracy dual latent space model, and provides
 183 a comparison of single latent space models and uncertainty quantification in the physical flow parameter
 184 prediction.

185 3.1 Dual AutoEncoder Performance

186 The DAS and DTS AEs are trained separately using an NVIDIA RTX 3080 GPU. Each AE has a total of
187 45,333 parameters. We train each AE for 150 epochs with a batch size of 10, using a validation split of
188 20%. Only one experimental trial is used to train the AEs, and we test the performance using the other
189 experimental trials. The total training time required for each AE is approximately 2 minutes and 20 seconds.
190 We use the Adam optimizer [28] with learning rate 1×10^{-3} , and a Mean Squared Error (MSE) loss function.
191 The training and validation performance per epoch for the DAS and DTS AEs is shown in Figure 10. We
192 observe minimal overfit in the validation set, corresponding to good model generalizability and reconstruction
193 accuracy for the DAS and DTS data. The models are then capable of predicting the reconstructed DAS and
194 DTS measurements extremely fast and accurately. To quantify the prediction accuracy, we use the structural
195 similarity index measure (SSIM) [29], MSE, and Peak Signal-to-Noise Ratio (PSNR) of the true and predicted
196 physical flow properties. SSIM provides a perceptual image-to-image comparison of luminance, contrast, and
197 structure, while MSE provides a pixel-wise intensity comparison. In the case of DAS predictions, we obtain
198 an SSIM of 94.68, MSE of 1.49×10^{-2} , and PSNR of 24.3 dB. For DTS predictions, we obtain an SSIM
199 of 94.37, MSE of 8.34×10^{-3} , and PSNR of 26.81 dB. Figures 11 and 12 show the original DAS and DTS
200 measurements used for training, their reconstructions, the absolute error, and a visualization of the latent
201 space, respectively.

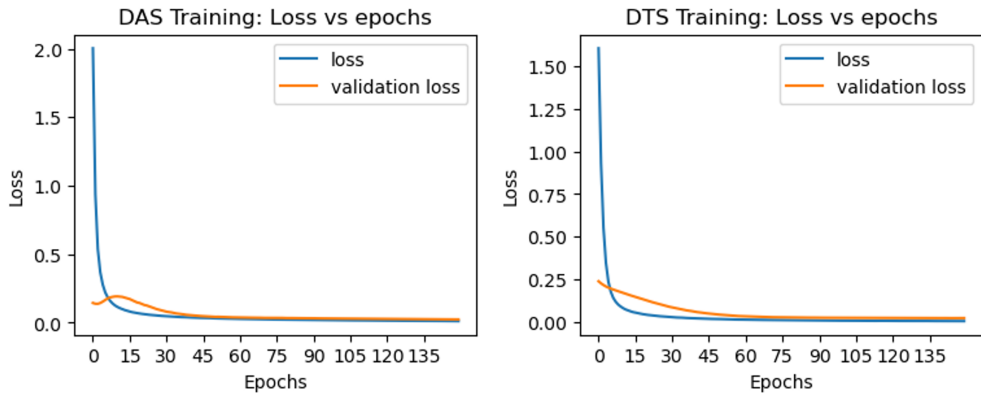


Figure 10: The total training and validation losses, \mathcal{L} , as a function of epoch number.

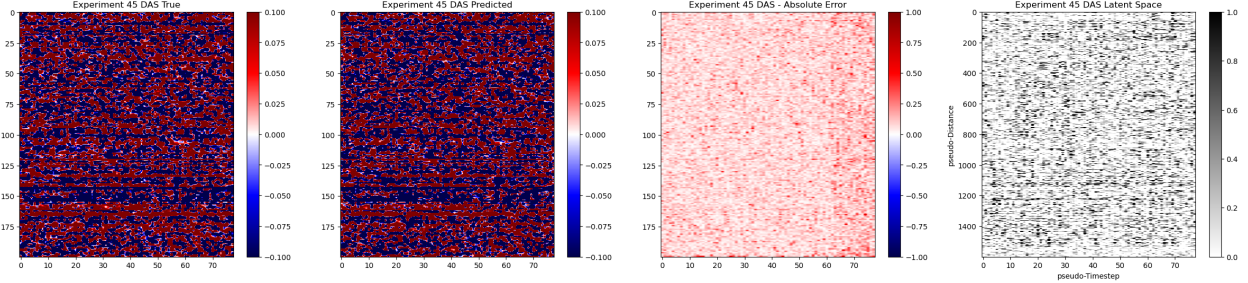


Figure 11: DAS AutoEncoder results for a training realization. (A) shows the normalized DAS data, (B) shows the reconstructed DAS, (C) shows the absolute error, and (D) shows a visualization of the DAS latent space for this training realization.

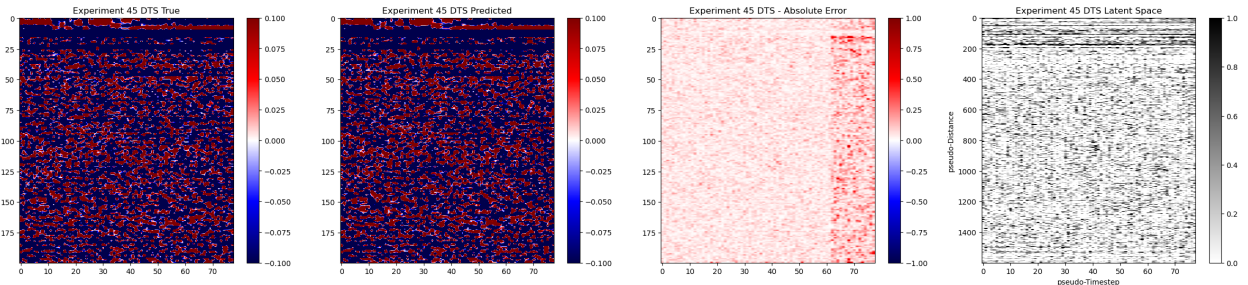


Figure 12: DTS AutoEncoder results for a training realization. (A) shows the normalized DTS data, (B) shows the reconstructed DTS, (C) shows the absolute error, and (D) shows a visualization of the DTS latent space for this training realization.

202 3.2 Flow Property Estimation

203 Once we have trained DAS and DTS AEs, we can extract the pre-trained Encoders and utilize them to
 204 construct dual latent spaces for the other experimental trials that were not used in the training procedure.
 205 Given that the DAS and DTS measurements have a dimensionality of approximately (200, 80), and the
 206 physical flow properties have a dimensionality of (200, 4), the estimation of the physical flow properties
 207 yields a highly over-determined inverse problem. Therefore, we choose to train a simple ℓ_2 -regularized linear
 208 model to predict the physical flow properties from the dual latent space. This can be expressed as:

$$\hat{y} = \|f(z^*) - y\|_2^2 + \lambda \|z^*\|_2^2, \quad (6)$$

209 where λ is the regularization weight, defined empirically as $\lambda = 2$.

210 We trained the dual latent space model with data from Trial 109, given that it contains measurements
 211 from all four phases (oil, water, gas, and sand). We then test the method with the other experimental trials.
 212 In other words, we train the DAS and DTS AEs with data from Trial 109, and use the pre-trained Encoders
 213 to compress the DAS and DTS measurements from the other trials and estimate the corresponding physical

214 flow properties. Figure 13 shows the true and predicted physical flow properties from the test trials, and
215 Table 2 presents the prediction accuracy metrics.

Table 2: Accuracy metrics for physical flow property prediction for test cases.

Trial Number	45	48	54	64	128
MSE	3.68×10^{-9}	3.55×10^{-9}	2.72×10^{-9}	3.61×10^{-9}	3.92×10^{-9}
SSIM	99.98	99.98	99.99	99.98	99.97

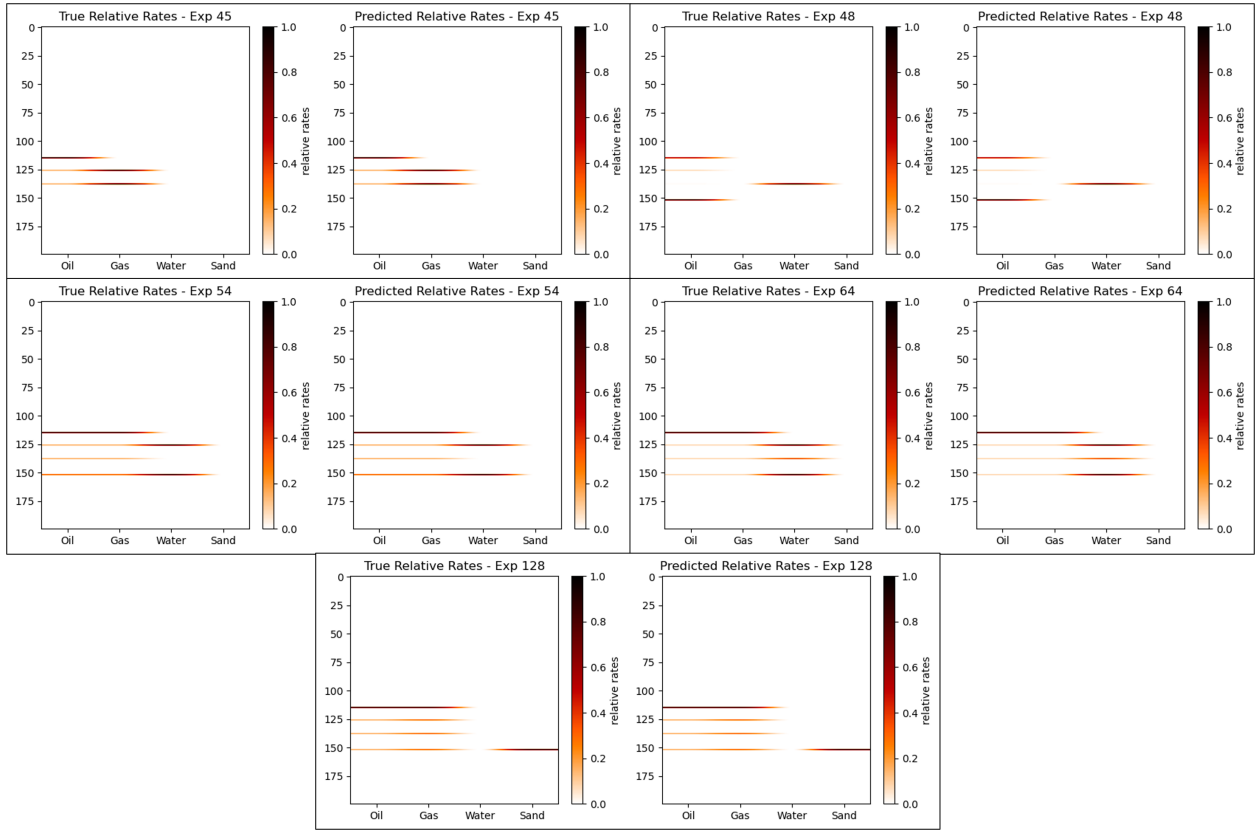


Figure 13: True and predicted physical flow properties for test realizations.

216 3.3 Dual vs. Single Latent Space

217 Given that the problem of estimating the physical flow properties from the DAS and DTS data is a highly
218 over-determined inverse problem, we also test the prediction performance of using a single latent space model
219 as opposed to our dual latent space model.

220 Using the pre-trained DAS and DTS Encoders, Enc_{θ_i} , we construct a single latent space representation
221 of the DAS and DTS data, respectively, and use it to estimate the physical flow properties in each test
222 trial. Namely, $\hat{y}_i = f(z_i) = f(Enc_{\theta_i}(X_i))$, as opposed to the proposed dual latent space model case where

223 $\hat{y} = f(z^*) = f([Enc_{\theta_1}(X_{DAS}), Enc_{\theta_2}(X_{DTS})])$. Figures 14, 15, and 16 compares the prediction using a
 224 single latent space representation with DAS measurements, a single latent space representation with DTS
 225 measurements, and the proposed dual latent space model for the test trials 45, 64, and 128, respectively.
 226 Table 3 shows the prediction accuracy metrics for the three scenarios of all of the five test cases.

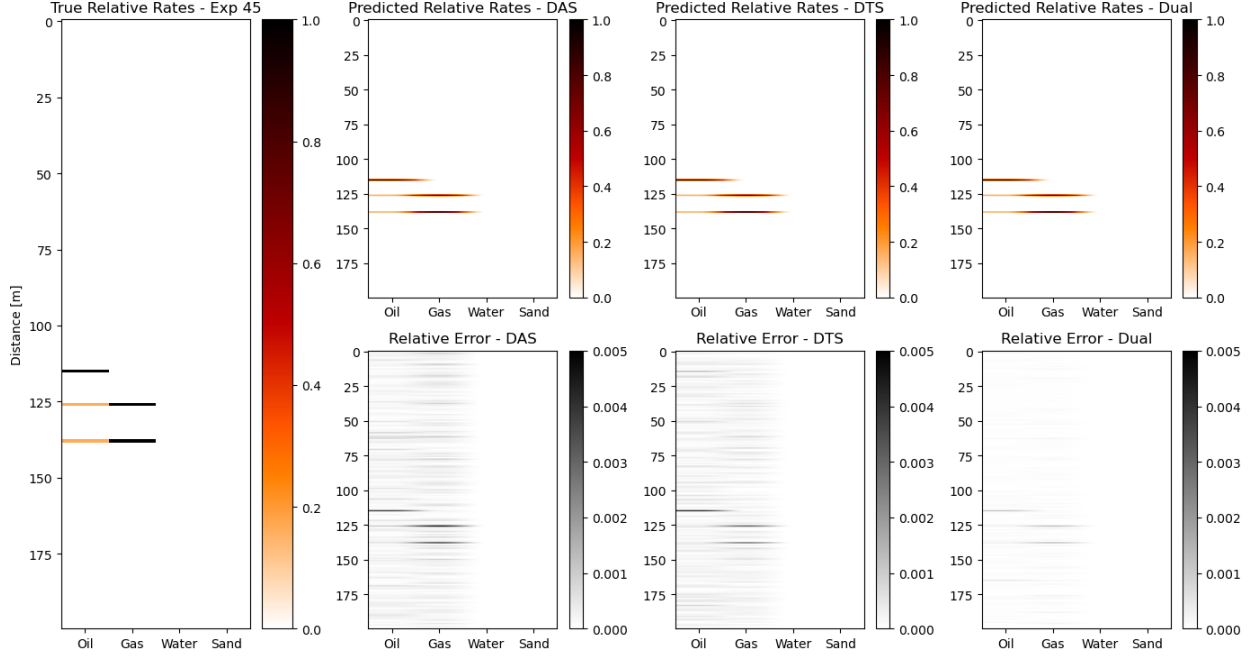


Figure 14: Comparison of single and dual latent space models for Trial 45; (A) is the true relative rates, (B) is the single-DAS prediction, (C) is the single-DTS prediction, and (D) is the dual latent space prediction.

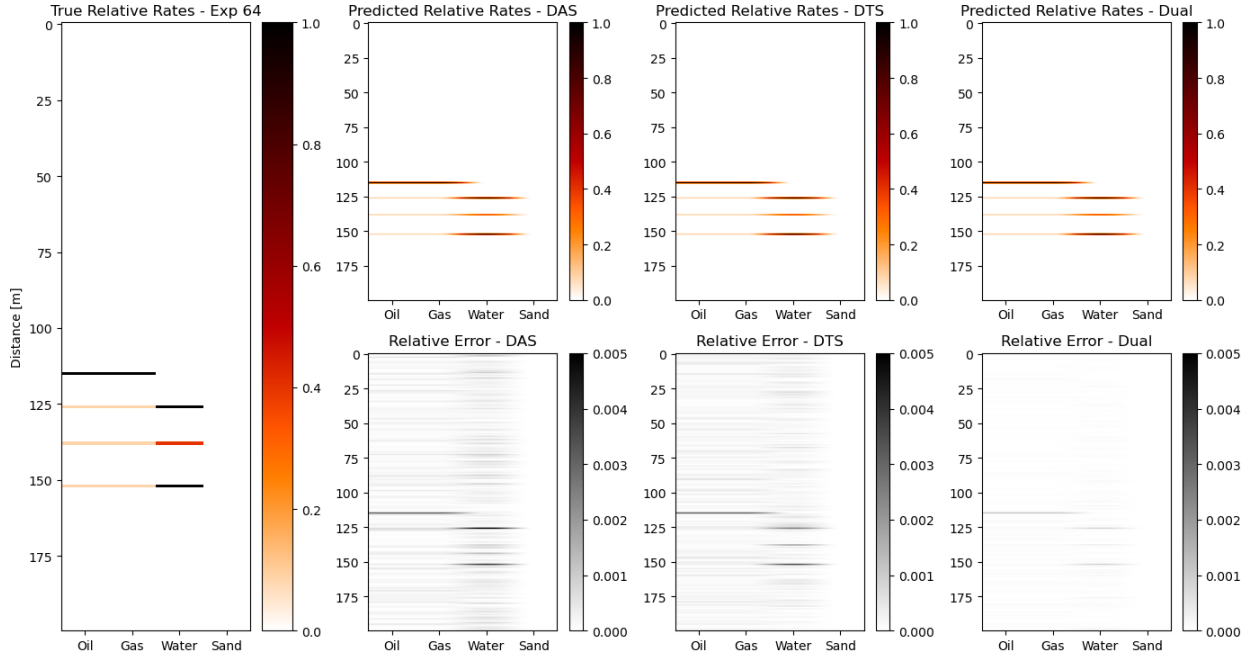


Figure 15: Comparison of single and dual latent space models for Trial 64; (A) is the true relative rates, (B) is the single-DAS prediction, (C) is the single-DTS prediction, and (D) is the dual latent space prediction.

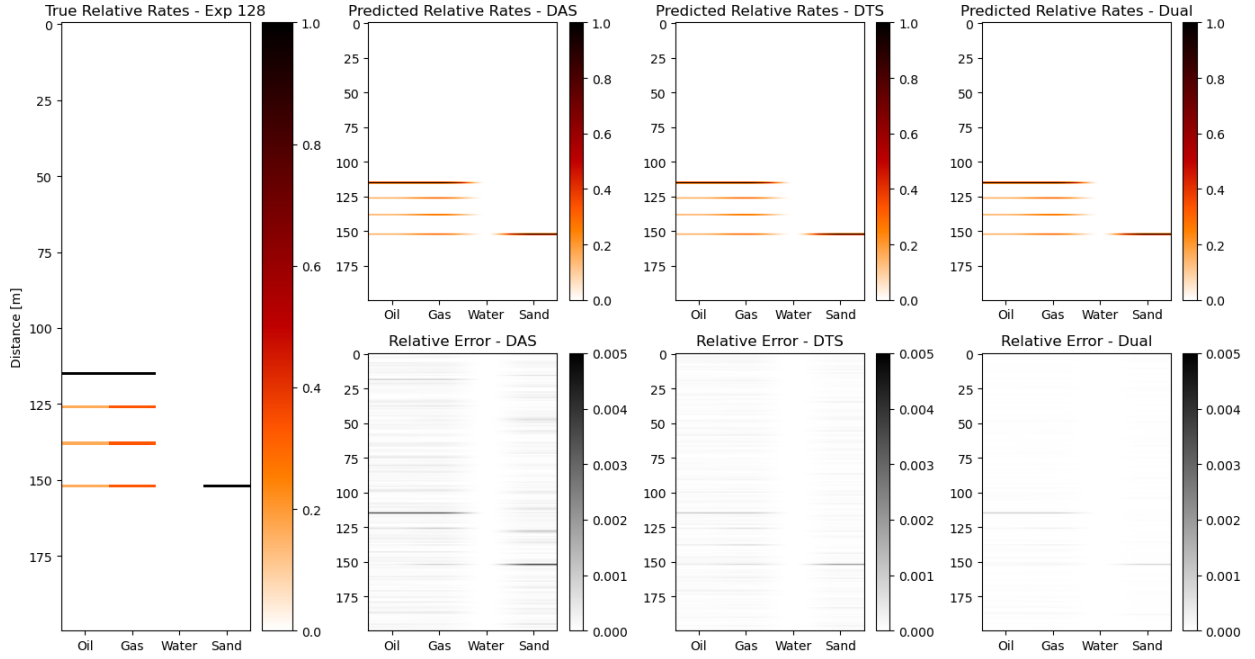


Figure 16: Comparison of single and dual latent space models for Trial 128; (A) is the true relative rates, (B) is the single-DAS prediction, (C) is the single-DTS prediction, and (D) is the dual latent space prediction.

Table 3: Prediction accuracy metrics for all test trials using single DAS latent space, single DTS latent space, and Dual latent space models.

Trial Number	Latent Representation	MSE	SSIM
45	DAS	9.82×10^{-8}	99.95
	DTS	6.97×10^{-8}	99.96
	Dual	3.68×10^{-9}	99.98
48	DAS	7.93×10^{-8}	99.96
	DTS	4.41×10^{-8}	99.97
	Dual	3.55×10^{-9}	99.98
54	DAS	8.20×10^{-8}	99.96
	DTS	2.52×10^{-8}	99.97
	Dual	2.72×10^{-9}	99.99
64	DAS	1.29×10^{-7}	99.93
	DTS	8.29×10^{-8}	99.95
	Dual	3.61×10^{-9}	99.98
128	DAS	7.04×10^{-8}	99.95
	DTS	1.52×10^{-8}	99.96
	Dual	3.92×10^{-9}	99.97

227 3.4 Uncertainty Quantification

228 Naturally, DAS and DTS measurements are very noisy in nature due to the subsurface and operational
 229 conditions. Therefore, we decide to quantify the uncertainty in our physical flow property predictions by
 230 adding different levels of random noise to the DAS and DTS data in our dual latent space model. Let ε be
 231 the random noise, such that $\varepsilon \sim \mathcal{N}(0, \sigma_i)$, where σ_i is the standard deviation of the original DAS or DTS
 232 data, X_i . The noisy DAS and DTS measurements are given by $\tilde{X}_i = X + p * \varepsilon$, where p is the percent
 233 noise added. We quantify the uncertainty with in our predictions with 5%, 10%, 25%, and 50% added noise.
 234 Figures 17, 18, and 19 show the results in estimating physical flow properties by of adding different levels of
 235 noise to the dual latent space model.

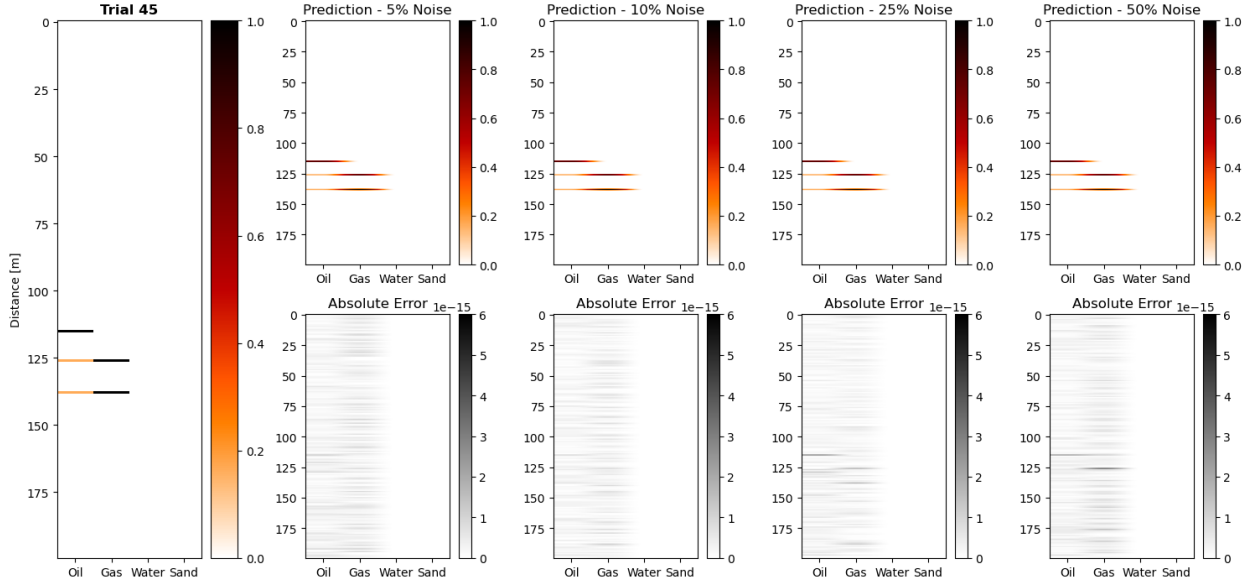


Figure 17: Prediction of physical flow properties for Trial 45 with different levels of added noise; (A) is the true relative rates, (B) 5% noise, (C) 10% noise, (D) 25% noise, and (E) 50% noise. The top row shows the estimated physical flow properties, and the bottom row shows the absolute error.

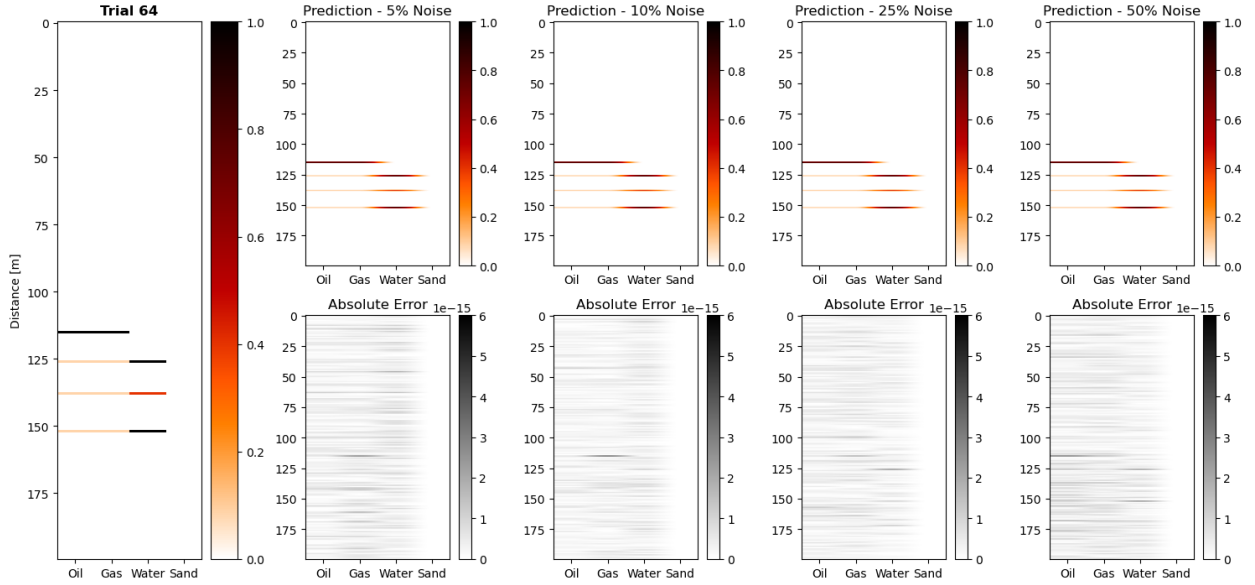


Figure 18: Prediction of physical flow properties for Trial 64 with different levels of added noise; (A) is the true relative rates, (B) 5% noise, (C) 10% noise, (D) 25% noise, and (E) 50% noise. The top row shows the estimated physical flow properties, and the bottom row shows the absolute error.

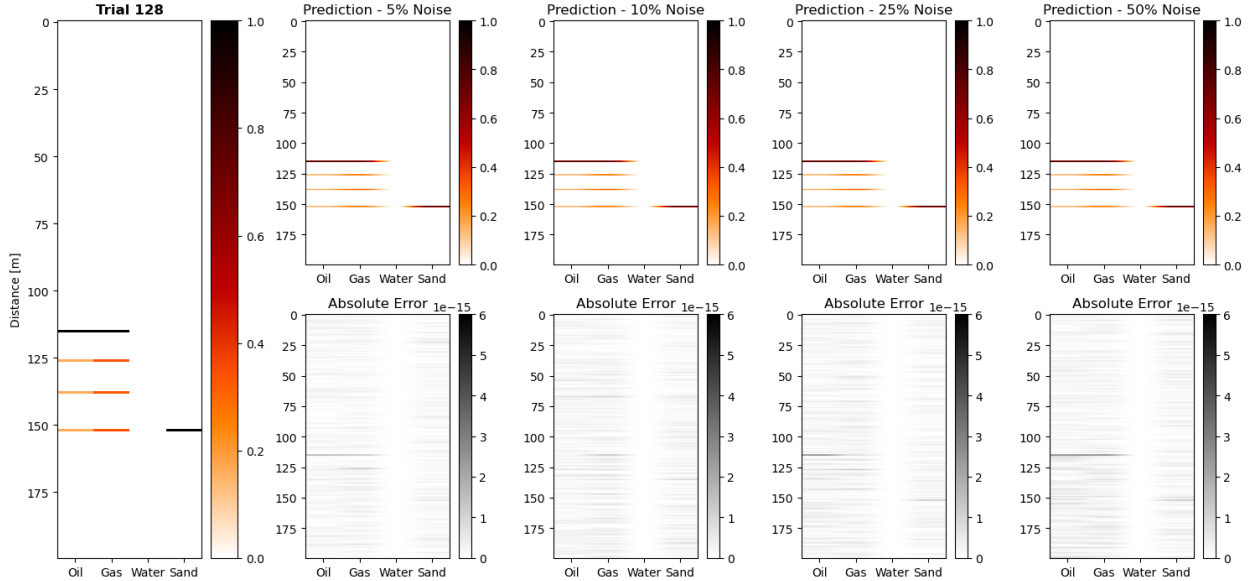


Figure 19: Prediction of physical flow properties for Trial 128 with different levels of added noise; (A) is the true relative rates, (B) 5% noise, (C) 10% noise, (D) 25% noise, and (E) 50% noise. The top row shows the estimated physical flow properties, and the bottom row shows the absolute error.

236 3.5 Discussion

237 Our proposed dual latent space model provides accurate and computationally efficient predictions of physical
 238 flow properties from DFOS measurements. The proposed method is capable of estimating the injection
 239 point location and relative multiphase flow rates within 7-9 significant figures, in under 10 milliseconds.
 240 The entire workflow, including the data processing, resampling, model training, and property prediction,
 241 takes approximately 4.44 seconds on an Intel i9-10900K CPU. This provides an opportunity for real time
 242 monitoring using DFOS measurements with frequent re-processing and re-training to continuously improve
 243 model performance.

244 Furthermore, the problem of estimating physical flow properties from DFOS measurements is posed as
 245 a highly over-determined inverse problem. This implies that the entire DAS and DTS data is not required
 246 to accurately predict the injection point locations and relative multiphase flow rates, and that a latent rep-
 247 resentation of the data is sufficient and more effective for real-time predictions. After processing, the DFOS
 248 measurements are compressed to approximately 0.003% of the raw data size. Their latent representations,
 249 z_{DAS} and z_{DTS} , apply a further 25% reduction in dimensionality. In practice, the processing and encoding
 250 stage would be performed at the source, while the decoding stage would be performed in the cloud. In
 251 this setup, a highly-compressed and accurate latent representation is necessary for efficient data streaming
 252 through an internet connection from the field to the end users.

Comparing the single latent space models to the dual latent space model, we observe a slight advantage when combining both DAS and DTS data into the estimation of the physical flow properties. However, given that the estimation problem is highly over-determined, a single latent space model could still be useful for a wide array of applications. The difference in terms of accuracy is between 1 and 2 orders of magnitude, yet still very small, in the order of 10^{-7} - 10^{-9} . Furthermore, there is no noticeable computational savings when using a single or dual latent space model, given that the DAS and DTS Encoders are both pre-trained and provide the latent representations in less than 10 milliseconds.

Moreover, the dual latent space model shows robustness to noise. Given that DAS and DTS measurements are very noisy in nature, adding further noise does not affect significantly the accuracy of the predictions. The Encoder networks show robustness to noise, and are still capable of extracting the salient latent features in the DAS and DTS measurements despite increasing levels of noise. This is promising due to the fact that our dual latent space model is trained with measurements from a controlled flow-loop experiment and subsurface applications are more likely to include higher noise levels.

4 Conclusions

We present a novel deep learning-based architecture for the prediction of injection points and relative rates based on distributed fiber optic sensing measurements. The proposed methodology exploits the spatiotemporal latent space from time-lapse DAS and DTS measurements through a double-U-Net architecture. Measurements from controlled flow-loop experiments with multiphase flow are used to train the network and extract acoustic and temperature latent spaces. These are combined in order to accurately predict the points of injection along the flow-loop as well as the relative rates of each phase passing through the perforations.

The double-U-Net architecture is designed in a modular fashion, with one convolutional U-net AutoEncoder for the time-lapse DAS data and a separate convolutional U-net AutoEncoder for the time-lapse DTS data. However, both AutoEncoders are exactly the same in terms of architecture but trained separately due to the difference in sampling rate of the two signals. The AutoEncoders are designed with four convolutional blocks encoding the data into a latent space and four transpose convolutional blocks, which are concatenated to the original encoder blocks using residual concatenations, onto the decoded time-lapse signal. The parameters are trained to minimize the difference between the original and reconstructed signals. The Encoder portions of the two architecture are extracted and used to generate the acoustic and temperature latent spaces, respectively. A third estimator is designed to receive the combined latent space and predict a mask containing the injection locations and relative rates.

The entire training process required approximately 27 minutes on a single NVIDIA Quadro M6000 GPU.

284 Training is done with one experimental dataset, and testing is performed with different experimental data.
285 Errors are consistently below $3.68 \times 10^{-9}\%$ and signal similarity is over 98.9%. After the pre-training is
286 done, predictions of physical flow properties are obtained in under 10 milliseconds.

287 Therefore, this model can be used for real-time predictions and evaluation of subsurface energy systems
288 in applications such as oil and gas production, hydraulic fracturing monitoring, geologic carbon storage,
289 and geothermal energy production. To our knowledge, our work is the first to develop a methodology
290 for reduced-dimensional modeling of distributed fiber optic sensing data, and the prediction of injection
291 locations and relative rates through the enhanced latent space for accurate and real-time multiphase fluid
292 flow characterization. Future opportunities include varying the number and location of the injection points to
293 generate more training samples, applying a transfer learning protocol to predict the physical flow properties
294 on other subsurface scenarios (e.g., enhanced oil recovery, CO₂ sequestration), and deploying the model on
295 the cloud for real-time processing instead of post-processing.

296 **Reproducibility**

297 The code will be made publicly available on the author's repository (github.com/misaelmmorales).

298 **Funding**

299 This research did not receive any specific grant from funding agencies in the public, or not-for-profit sectors.

300 **Declarations**

301 The authors declare no conflict of interests.

302 **Acknowledgements**

303 The authors thank Martin Sundin and Çagri Cerrahoglu of Lytt for their support and insights. The authors
304 would also like to thank the Formation Evaluation (FE) and Digital Reservoir Characterization Technology
305 (DIRECT) Industry Affiliate Programs at the University of Texas at Austin for supporting this work.

306 **References**

- 307 [1] Bin Luo, Ariel Lellouch, Ge Jin, Biondo Biondi, and James Simmons. Seismic inversion of shale reservoir properties using microseismic-induced guided waves recorded by distributed acoustic sensing. *Geophysics*, 86(4):R383–R397, 2021.
- 310 [2] Fuad Aziz Atakishiyev, Alessandro Delfino, Cagri Cerrahoglu, Zahid Hasanov, Ilkin Yusifov, Alex Wallace, and Alberto Mendoza. Flow Diagnostics in High Rate Gas Condensate Well Using Distributed Fiber-Optic Sensing and its Validation with Conventional Production Log. volume Day 1 Tue, September 07, 2021 of *SPE Offshore Europe Conference and Exhibition*, page D011S002R002, 09 2021. doi: 10.2118/205435-MS.
- 315 [3] Abhishek Venketeswaran, Nageswara Lalam, Jeffrey Wuenschell, Paul R Ohodnicki Jr, Mudabbir Badar, Kevin P Chen, Ping Lu, Yuhua Duan, Benjamin Chorpeling, and Michael Buric. Recent advances in machine learning for fiber optic sensor applications. *Advanced Intelligent Systems*, 4(1):2100067, 2022.
- 318 [4] A Mateeva, J Lopez, D Chalenski, M Tatanova, P Zwartjes, Z Yang, S Bakku, K de Vos, and H Potters. 4d das vsp as a tool for frequent seismic monitoring in deep water. *The Leading Edge*, 36(12):995–1000, 2017.
- 321 [5] Paul Zwartjes, Albena Mateeva, David Chalenski, Yuting Duan, Denis Kiyashchenko, and Jorge Lopez. Frequent, multi-well, stand-alone 3d das vsp for low-cost reservoir monitoring in deepwater. In *SEG Technical Program Expanded Abstracts 2018*, pages 4948–4952. Society of Exploration Geophysicists, 2018.
- 325 [6] Zahid Hasanov, Parviz Allahverdiyev, Fuad Ibrahimov, Alberto Mendoza, Pradyumna Thiruvengatathan, Lilia Noble, and Jonathan Stapley. Production Optimization of Sanding Horizontal Wells Using a Distributed Acoustic Sensing (DAS) Sand Monitoring System: A Case Study From the ACG Field in Azerbaijan. volume Day 1 Mon, May 17, 2021 of *SPWLA Annual Logging Symposium*, page D011S001R001, 05 2021. doi: 10.30632/SPWLA-2021-0001.
- 330 [7] Rolf Birger Pedersen, LJ Reigstad, and T Baumberger. Scientific cruise to the sleipner area in the north sea; r/v go sars expedition no. 2012108/cgb2012, june 22th-30th 2012, bergen, norway-bergen, norway. 2012.
- 333 [8] Islam Ashry, Yuan Mao, Biwei Wang, Frode Hvæding, Ahmed Y Bukhamsin, Tien Khee Ng, and Boon S Ooi. A review of distributed fiber-optic sensing in the oil and gas industry. *Journal of Lightwave Technology*, 40(5):1407–1431, 2022.

- 336 [9] Daniele Inaudi and Branko Glisic. Fiber optic sensing for innovative oil & gas production and transport
337 systems. In *Optical Fiber Sensors*, page FB3. Optica Publishing Group, 2006.
- 338 [10] Thomas M Daley, Barry M Freifeld, Jonathan Ajo-Franklin, Shan Dou, Roman Pevzner, Valeriya Shu-
339 lakova, Sudhendu Kashikar, Douglas E Miller, Julia Goetz, Jan Henninges, et al. Field testing of
340 fiber-optic distributed acoustic sensing (das) for subsurface seismic monitoring. *The Leading Edge*, 32
341 (6):699–706, 2013.
- 342 [11] Derrick Chambers, Ge Jin, Ahmad Tourei, Abdul Hafiz Saeed Issah, Ariel Lellouch, Eileen Martin,
343 Donglin Zhu, Aaron Girard, Shihao Yuan, Thomas Cullison, et al. Dascore: a python library for
344 distributed fiber optic sensing. *EarthArXiv*, 2024. doi: <https://doi.org/10.31223/X5B978>.
- 345 [12] Hasan Asy’ari Arief, Tomasz Wiktorski, and Peter James Thomas. A survey on distributed fibre optic
346 sensor data modelling techniques and machine learning algorithms for multiphase fluid flow estimation.
347 *Sensors*, 21(8):2801, 2021.
- 348 [13] CS Sherman, RJ Mellors, and JP Morris. Subsurface monitoring via physics-informed deep neural
349 network analysis of das. In *ARMA US Rock Mechanics/Geomechanics Symposium*, pages ARMA–2019.
350 ARMA, 2019.
- 351 [14] Vincent Dumont, Verónica Rodríguez Tribaldos, Jonathan Ajo-Franklin, and Kesheng Wu. Deep learning
352 for surface wave identification in distributed acoustic sensing data. In *2020 ieee international
353 conference on big data (big data)*, pages 1293–1300. IEEE, 2020.
- 354 [15] Steven L Brunton, Joshua L Proctor, and J Nathan Kutz. Discovering governing equations from data by
355 sparse identification of nonlinear dynamical systems. *Proceedings of the national academy of sciences*,
356 113(15):3932–3937, 2016.
- 357 [16] William D Fries, Xiaolong He, and Youngsoo Choi. Lasdi: Parametric latent space dynamics identifi-
358 cation. *Computer Methods in Applied Mechanics and Engineering*, 399:115436, 2022.
- 359 [17] Vincent Dumont, Verónica Rodríguez Tribaldos, Jonathan Ajo-Franklin, and Kesheng Wu. Deep learn-
360 ing on real geophysical data: A case study for distributed acoustic sensing research. *arXiv preprint
361 arXiv:2010.07842*, 2020.
- 362 [18] Yankun Sun, Jinquan Liu, Ziqiu Xue, Qi Li, Chengkai Fan, and Xu Zhang. A critical review of dis-
363 tributed fiber optic sensing for real-time monitoring geologic co2 sequestration. *Journal of Natural Gas
364 Science and Engineering*, 88:103751, 2021.

- 365 [19] Teymur Sadigov, Cagri Cerrahoglu, James Ramsay, Laurence Burchell, Sean Cavalero, Thomas Watson,
366 Pradyumna Thiruvenkatanathan, and Martin Sundin. Real-time water injection monitoring with
367 distributed fiber optics using physics-informed machine learning. In *Offshore Technology Conference*,
368 page D041S054R007. OTC, 2021.
- 369 [20] Shuvajit Bhattacharya, Payam Kavousi Ghahfarokhi, Timothy R Carr, and Scott Pantaleone. Application
370 of predictive data analytics to model daily hydrocarbon production using petrophysical, geomechanical,
371 fiber-optic, completions, and surface data: A case study from the marcellus shale, north
372 america. *Journal of Petroleum Science and Engineering*, 176:702–715, 2019.
- 373 [21] Zhaoqiang Peng, Jianan Jian, Hongqiao Wen, Andrei Gribok, Mohan Wang, Hu Liu, Sheng Huang,
374 Zhi-Hong Mao, and Kevin P Chen. Distributed fiber sensor and machine learning data analytics for
375 pipeline protection against extrinsic intrusions and intrinsic corosions. *Optics Express*, 28(19):27277–
376 27292, 2020.
- 377 [22] King Ma, Henry Leung, Ehsan Jalilian, and Daniel Huang. Fiber-optic acoustic-based disturbance
378 prediction in pipelines using deep learning. *IEEE Sensors Letters*, 1(6):1–4, 2017.
- 379 [23] Fantine Huot, Ariel Lellouch, Paige Given, Bin Luo, Robert G Clapp, Tamas Nemeth, Kurt T Nihei,
380 and Biondo L Biondi. Detection and characterization of microseismic events from fiber-optic das data
381 using deep learning. *Seismological Society of America*, 93(5):2543–2553, 2022.
- 382 [24] Alberto Mendoza, Çagri Cerrahoglu, Alessandro Delfino, and Martin Sundin. Signal processing and
383 machine learning for effective integration of distributed fiber optic sensing data in production petrophysics.
384 In *SPWLA Annual Logging Symposium*, page D031S003R006. SPWLA, 2022.
- 385 [25] Pradyumna Thiruvenkatanathan, Tommy Langnes, Paul Beaumont, Daniel White, and Michael Webster.
386 Downhole Sand Ingress Detection Using Fibre-Optic Distributed Acoustic Sensors. Abu Dhabi
387 International Petroleum Exhibition and Conference, page D031S061R002, 11 2016. doi: 10.2118/
388 183329-MS.
- 389 [26] MD McKay, RJ Beckman, and WJ Conover. A comparison of three methods for selecting values of
390 input variables in the analysis of output from a computer code. *Technometrics*, 21:239–245, 1979.
- 391 [27] Olaf Ronneberger, Philipp Fischer, and Thomas Brox. U-net: Convolutional networks for biomedical
392 image segmentation. In *Medical Image Computing and Computer-Assisted Intervention–MICCAI 2015: 18th
393 International Conference, Munich, Germany, October 5–9, 2015, Proceedings, Part III 18*, pages
394 234–241. Springer, 2015.

395 [28] Diederik P Kingma and Jimmy Ba. Adam: A method for stochastic optimization. *arXiv preprint*
396 *arXiv:1412.6980*, 2014.

397 [29] Zhou Wang, Alan C Bovik, Hamid R Sheikh, and Eero P Simoncelli. Image quality assessment: from
398 error visibility to structural similarity. *IEEE transactions on image processing*, 13(4):600–612, 2004.